Computer Modeling in Engineering & Sciences CMES, vol.122, no.2, pp.633-659, 2020

Experimental Simulation and Numerical Modeling of Deformation and Damage Evolution of Pre-Holed Sandstones After Heat Treatment

Shuo Yang[1], Yuanhai Li[1, 2, *], Xiaojie Tang[1, 2] and Jinshan Liu[1, 2]

Abstract: The deformation and damage evolution of sandstone after heat treatment greatly influence the efficient and safe development of deep geothermal energy extraction. To investigate this issue, laboratory confined compression tests and numerical simulations were conducted on pre-holed sandstone specimens after heat treatment. The laboratory test results show that the failure modes are closely related to the heat treatment temperature, with increasing treatment temperature, the failure modes change from mixed and shear modes to a splitting mode. The cracks always initiate from the sidewalls of the hole and then propagate. The failure process inside the hole proceeds as follows: calm period, particle ejection period, rock fragment exfoliation period and rock failure period. The specimens have different final failure features for the entire rock after heat treatment, but have the same failure features inside the hole. These phenomena can be explained by numerical simulations. The numerical simulations reveal that the failure modes in the numerical results agree very well with those observed in the experimental results. The damage zone always occurs at sidewalls of the hole and then propagates to the entire rock affected by shear or tensile damage. From 20°C to 200°C, thermal effect may promote shear damage and restrain tensile damage, while from 200°C to 800°C, thermal effect promotes tensile damage and restrains shear damage. Notably, the damage zone near the sidewalls of the hole has the same distribution range and pattern. Finally, the differences in the mechanisms due to increasing heat temperature are evaluated using scanning electron microscope (SEM) observations.

Keywords: Pre-holed sandstone, high temperature, confined compression, damage evolution, numerical modeling.

1 Introduction

Geothermal energy is widely recommended and is regarded as a renewable alternative energy source [Kumari, Ranjith, Perera et al. (2017); Martín-Gamboa, Iribarren, Dufour et

[1] State Key Laboratory for Geomechanics and Deep Underground Engineering, China University of Mining and Technology, Xuzhou, China.

[2] School of Mechanics and Civil Engineering, China University of Mining and Technology, Xuzhou, China.

[*] Corresponding Author: Yuanhai Li. Email: Lyh@cumt.edu.cn.

Received: 10 July 2019; Accepted: 25 September 2019.

al. (2015)]. Sandstone usually serves as a geothermal reservoir buried deeply underground, and the deformation and damage evolution of sandstone after heat treatment greatly influence the efficient and safe development of deep geothermal energy extraction [Minissale, Borrini, Montegrossi et al. (2008)] .

In recent years, the properties of sandstone have been widely investigated [Zhang, Deng, Taheri et al. (2018); Taheri, Royle, Yang et al. (2016)]. The variations in the peak strength during triaxial monotonic and cyclic compressive testing have been investigated, and the effects of freeze-thaw cycles and chemical erosion have been analyzed.

Many researchers have also investigated the influence of temperature on the mechanical behavior of rocks under uniaxial [Dwivedi, Goel, Prasad et al. (2008); Heuze (1983)] and triaxial [Akdag, Karakus, Taheri et al. (2018b); Mohamadi and Wan (2016); Su, Jing, Yin et al. (2017b); Yao, Rong, Zhou et al. (2016)] compression. However, the aforementioned studies were performed on intact specimens, and these specimens did not contain any flaws. Yin et al. [Yin, Li, Yin et al. (2012)] conducted static and dynamic experimental studies on sandstone after heat treatment. These researchers studied the influence of high temperature on the peak strength, peak strain and failure mode. Chen et al. [Chen, Ni, Shao et al. (2012)] conducted uniaxial compression and fatigue loading tests on granite specimens after heat treatments, they found that peak stress and elastic modulus decreased with increasing temperature, while the peak strain increased. Kong et al. [Kong, Wang, Li et al. (2016)] investigated the fracture mechanical behavior of sandstone after heat treatment; the results show that the increases in the acoustic emission (AE) counts rate and events at high temperature are greater than those at room temperature. Zhu et al. [Zhu, Tian, Jiang et al. (2018)] studied the effects of high temperature on the mechanical properties of Chinese marble; these researchers found that the effect of high temperature is mainly due to the change in the primary micro-cracks and the development of new micro-cracks from the thermal expansion of calcite and dolomite. Akdag et al. [Akdag, Karakus, Taheri et al. (2018b)] studied the thermal damage of brittle rocks under true-triaxial loading and unloading conditions; these researchers found that the strain burst stress, initial rock fragment ejection velocity, and kinetic energy decrease from room temperature to 100°C.

The fundamental properties of rocks with an existing hole have been widely investigated [Weng, Li, Taheri et al. (2018); Zeng, Yang and Tian (2018)]. Furthermore, the failure behavior of rock specimens containing pre-existing flaws after heat treatment has been widely investigated. However, these experiments were always limited to unconfined compression conditions. The above studies were performed without consideration of confined stress from surrounding rock, which affects the deformation failure behavior. For instance, Huang et al. [Huang, Yang, Tian et al. (2017)] investigated the physical and mechanical behavior of granite containing pre-existing holes after heat treatment. As the temperature increases, the peak strength first increases and then decreases, while the elastic modulus decreases. Yang et al. [Yang, Hang, Tian et al. (2019); Yang, Jiang, Huang et al. (2014)] studied the deformation failure behavior of rock specimens containing fissures under uniaxial compression. These researchers concluded that the relationship between the crack evolution process of red sandstone containing a single fissure and two parallel fissures was dependent on the temperature. The main strains are first concentrated at the tips of the pre-existing fissure, indicating that the first cracks will start from the

concentration of strain. Based on previous studies, these researchers all investigated the crack initiation, propagation, and coalescence behavior of rock after heat treatment, but ignored the evolution process of cracks inside the flaws.

Many studies [Gong, Si, Li et al. (2018); Haimson and Chang (2000); Kusui, Villaescusa and Funatsu (2016); Lee, Moon and Haimson (2015); Liu, Liang, Zhang et al. (2018); Huang, Liu, Jiang et al. (2019)] have investigated the rock failure behavior under confined compression at room temperature; these studies concluded that critical ratios of the compressive strength to the induced stress existed for critical instability stages such as rock spalling and pillar crushing adjacent to the flaws. The quiet period of the AE event rate and the sharp increase of the AE energy rate can be regarded as precursors to rock failure. Based on microscale analysis of failed sandstone specimens, these researchers found that microdamage (intra and transgranular microcracks) dominantly occurs at grains rather than strongly cemented grain contacts. Nevertheless, the laboratory experiments were all conducted without investigating the influence of temperature.

Many laboratory experiments have been conducted to investigate slabbing and rockburst after heat treatment under confined compression. For example, Su et al. [Su, Chen, Ju et al. (2018)] studied strainburst under different high temperatures using a true-triaxial rockburst test system. These researchers found that when the temperature increases from 30°C to 300°C, the kinetic energy of the ejected fragments rapidly increases. Chen et al. [Chen, Li, Zhang et al. (2014); Chen, Li, Li et al. (2018)] found that rockbursts occurring at high ground temperatures are more intense than those occurring at room temperature. However, limited research regarding the failure behavior of rock specimens containing pre-existing flaws has been performed.

Until now, under confined compression conditions, information regarding the deformation and damage evolution of pre-holed sandstone after heat treatment has been limited. In this study, first, confined compression tests were conducted on pre-heated sandstone specimens using a rock testing system. The physical mechanical properties of sandstone after heat treatment were investigated. The deformation and failure behavior of the specimens were analyzed based on the digital speckle correlation method (DSCM). Then, numerical simulations were conducted to explore the damage evolution of rock failure after heat treatment. Finally, the differences in the mechanisms due to increasing temperature were discussed through SEM observations.

2 Experimental material and test procedure

2.1 Experimental material and specimen preparation

The material used throughout this research was white sandstone collected from the city of Renshou in the Sichuan province of China (Fig. 1(a)). As shown in Fig. 1(b), according to the X-ray diffraction (XRD) analysis, the mineral components of the sandstone material tested were primarily quartz (82.8%), feldspar (3.1%), siderite (0.9%), calcite (0.2%), and clay minerals (13%).

The specimens were all machined in the same direction from the same block of sandstone material. The cuboid specimens were 150 mm wide, 150 mm long and 45 mm thick. Each specimen had a pre-existing flaw (hole) with a diameter of 40 mm machined by water

drilling. Five groups of rock specimens were made for the experiment at temperatures of 20, 200, 400, 600 and 800°C. In the current research, high-temperature treatment was administered to the specimens through a heating furnace using the following procedure. First, 4 groups of specimens were heated to the target temperatures (200, 400, 600 and 800°C) at a rate of 10°C/min, which was lower than that of a similar sandstone experiment [Yang, Jing, Huang et al. (2014)]. The reason for this difference is that the dimensions of the flaw in this study were larger than those in previous study, and to ensure the complete of the specimens, the temperature gradient should be lower. Then, the specimens were held at the target temperature for two hours. Finally, the specimens were naturally cooled to room temperature (20°C). As shown in Fig. 1(c), the color of the samples became darker at 400°C, and gradually changed to brown-red at temperature greater than 600°C. This result suggests that the mineral composition of the sandstones changed with the temperature, which is further analyzed in Section 5.

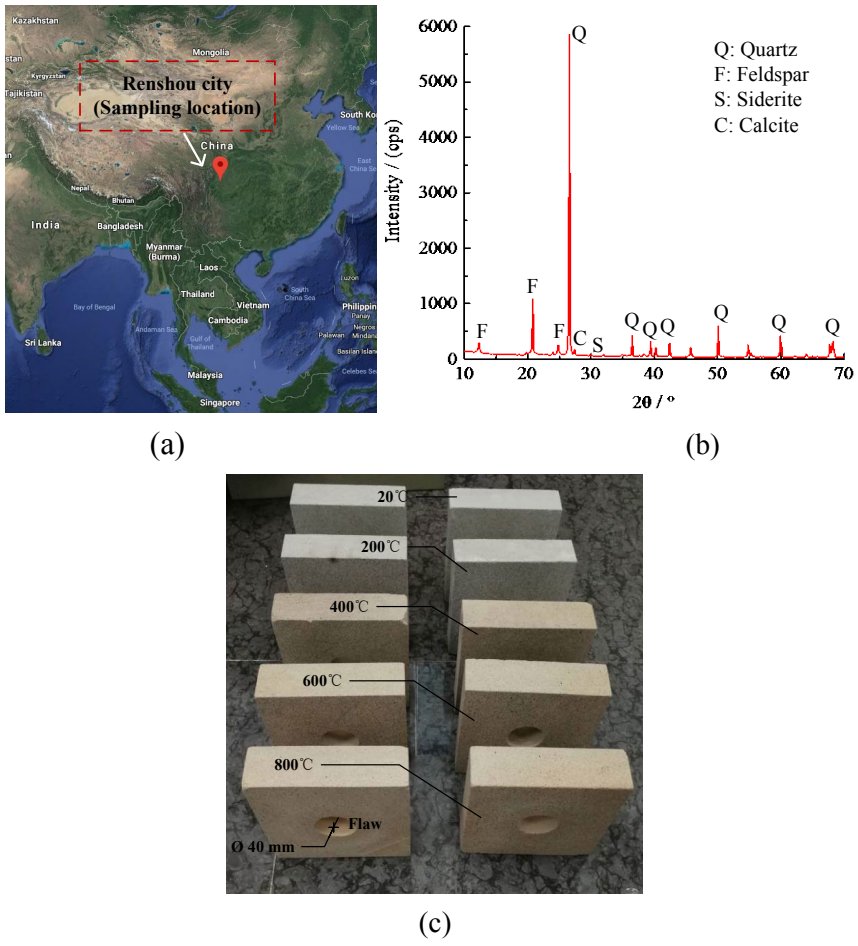

Figure 1: Sandstone specimens. (a) Sampling location, (b) XRD results for the sandstone material, and (c) test specimens treated with different temperatures

2.2 Testing system and procedure

As shown in Fig. 2(a), the testing system was composed of MTS816 rock mechanics servo-controlled testing system, a DSCM measuring system and an AE monitoring system. Specimens containing pre-existing holes and with heat-treated temperatures of 20°C, 200°C, 400°C, 600°C and 800°C were tested in the experiments. To simulate the surrounding rock boundary (Fig. 3), two rigid steel blocks were placed on two sides of the sample. As a lubricant, petroleum jelly was applied at the specimen-block interface to decrease the effects of platen restraint and end friction.

An axial force was imposed on the rock specimen surface under displacement-controlled conditions with a strain rate of 0.1 mm/min until failure occurred. The loads and deformations of specimens were simultaneously recorded at a data collection interval of 1 s. All the experiments were performed at the State Key Laboratory for Geomechanics and Deep Underground Engineering at the China University of Mining and Technology.

The acoustic emission equipment recorded the rock failure moment during the loading phase. An AE sensor was attached to the back of specimen near the pre-existing hole using a hot bar as a coupler and affixed with tape (Fig. 2(b)). The full waveforms of the AE signals were recorded during the test with the threshold set to 45 dB and the preamplifier set to 40 dB.

The DSCM measuring system was composed of a charge-coupled device (CCD) camera, an image acquisition control system, DSCM analysis software and a mobile graphics workstation.

The surface failure process of the specimens was captured by a CCD camera (Basler Aca4024-8gc) at rate of 8 frames per second. An image acquisition control system with a jumbo frame mode was used to process the high-speed and high-definition images.

Surface speckles were sprayed on the surfaces of the specimens for DSCM analysis [Chen, Yang, Pathegama et al. (2018); Zhao, Niu, Zhang et al. (2019); Zhao, Zhou, Zhao et al. (2018)], as shown in Fig. 3. Then, the rock-surface images captured were analyzed using the self-developed DSCM analysis software-PhotoInfor. The accuracies of the measurements by PhotoInfor has been demonstrated based on both theoretical analysis and experimental tests [Li, Tang, Yang et al. (2019)]. Moreover, a microcamera was placed behind the specimen to record the crack evolution process of the sidewalls of the hole in real-time (Fig. 2(b)).

In DSCM, fracture reduces the correlation coefficient, leading to errors. The OPFPM algorithm [Li, Zhang, Lin et al. (2016)] of PhotoInfor can be used to analyze the deformation of the surrounding rock while cracks appear. This method avoids the low image correlation caused by cracks. The principle of this algorithm is to find a pixel block that does not cross the crack and can avoid the low image correlation caused by the fracture. Therefore, the misjudgment of image pixels is reduced, and the deformation analysis accuracy is improved.

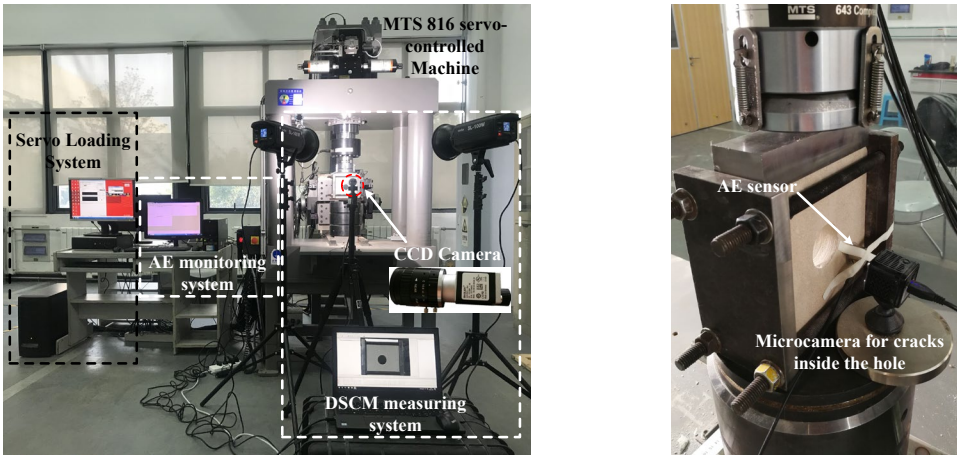

(a) (b)

Figure 2: Arrangement of the physical model experiment. (a) Front view of the experiment system and (b) back view of the specimen

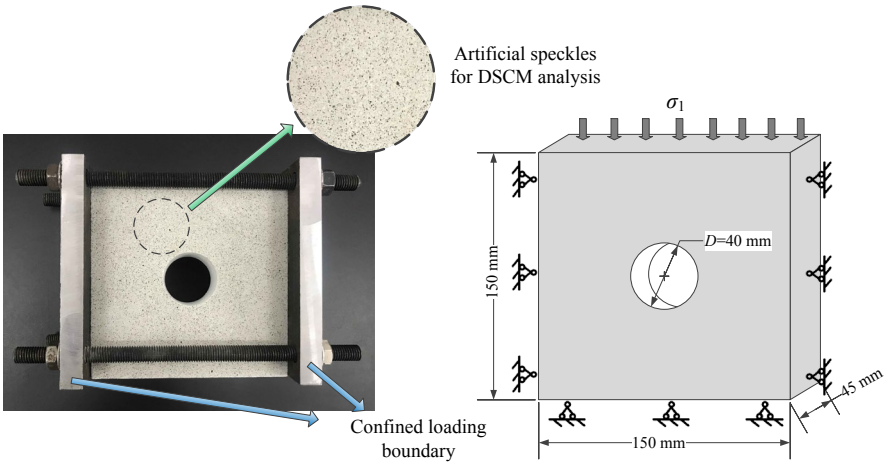

(a) (b)

Figure 3: Specimens for testing. (a) Artificial speckles for DSCM and (b) loading mode of specimens

3 Results of laboratory test

3.1 Effect of high temperature on mechanical properties

Fig. 4 shows the stress-strain curves of the pre-holed sandstone specimens after heat treatment. We noticed some interesting features from Fig. 4(a). For the room temperature and 200°C samples, the curve gradually decreases at the peak stage, exhibiting strain softening characteristics. However, when the temperature of the heat treatment is greater than 200°C, the curve abruptly decreases after the peak stage. The temperature influences the slope of the stress-strain curve and the peak strength. We analyzed this phenomenon is

in detail in the following. To obtain the best possible results, we conducted two experiments at each temperature. As shown in Figs. 4(b)-4(d), sample variability has little effect on the mechanical parameters (e.g., peak strength).

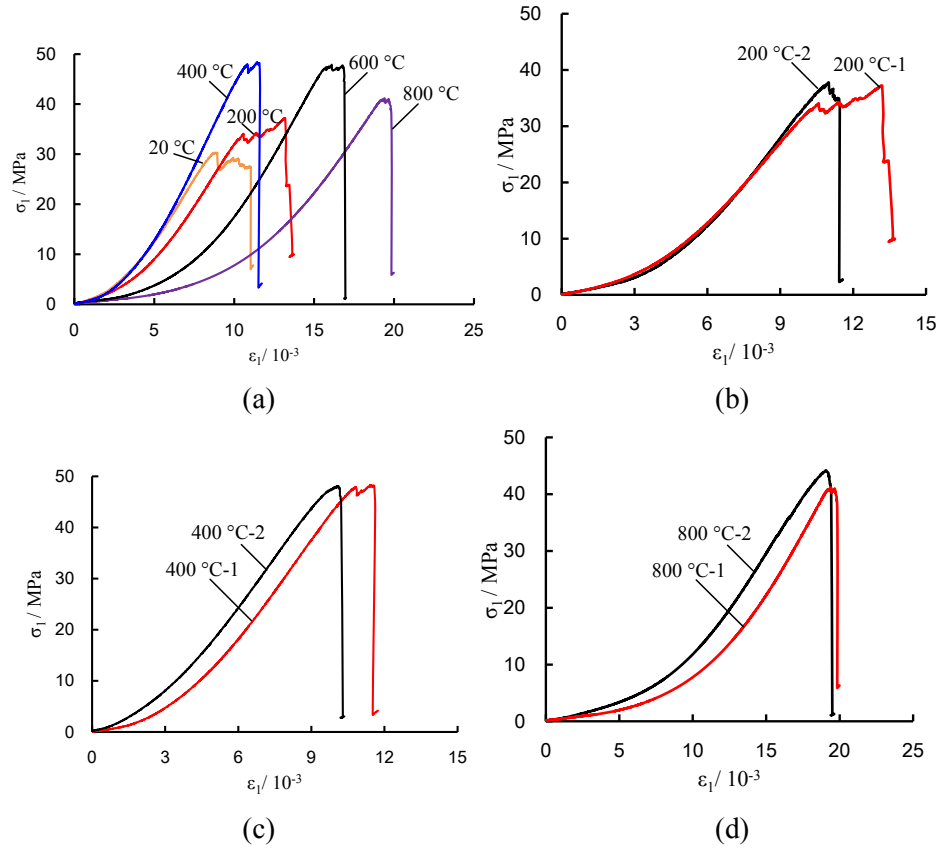

Figure 4: Stress-strain curves of pre-holed sandstone specimens after heat treatment. (a) Different temperatures, (b) same temperature (T=200°C), (c) same temperature (T=400°C) and (d) same temperature (T=800°C)

Fig. 5 shows the effects of high temperature on the strength and deformation parameters of the pre-holed sandstone specimens after heat treatment. Notably, the peak strength, peak strain and elastic modulus are related to high temperature, and the curves change nonlinearly with changing temperature. The peak strength and elastic modulus exhibit the same trend of first increasing and then decreasing. For the 400°C sample, both these parameters reach the maximum. The strengths of the specimens are strengthened by the high temperature, and the peak strength increases to 48.21 MPa. At 600°C, the peak strength increases to 48.73 MPa. The strength begins to decrease after the high temperature exceeds 600°C. A temperature of 600°C is the threshold for the strength transformation in this study.

The peak strain exhibits a different trend of a wave-like increase and reaches the maximum at a temperature of 800°C and minimum at a temperature of 400°C. Thus, 400°C may be the threshold temperature for the peak strain value. These mechanical parameters exhibit similar

trends in an experimental study by Zhu et al. [Zhu, Tian, Jiang et al. (2018)]. The temperature threshold is not similar to that of this study due to the different compression conditions.

These confined compression tests may possibly restrict microcrack propagation and increase the strength. Furthermore, compared with the strength and strain, the elastic modulus is the least affected by high-temperature treatment.

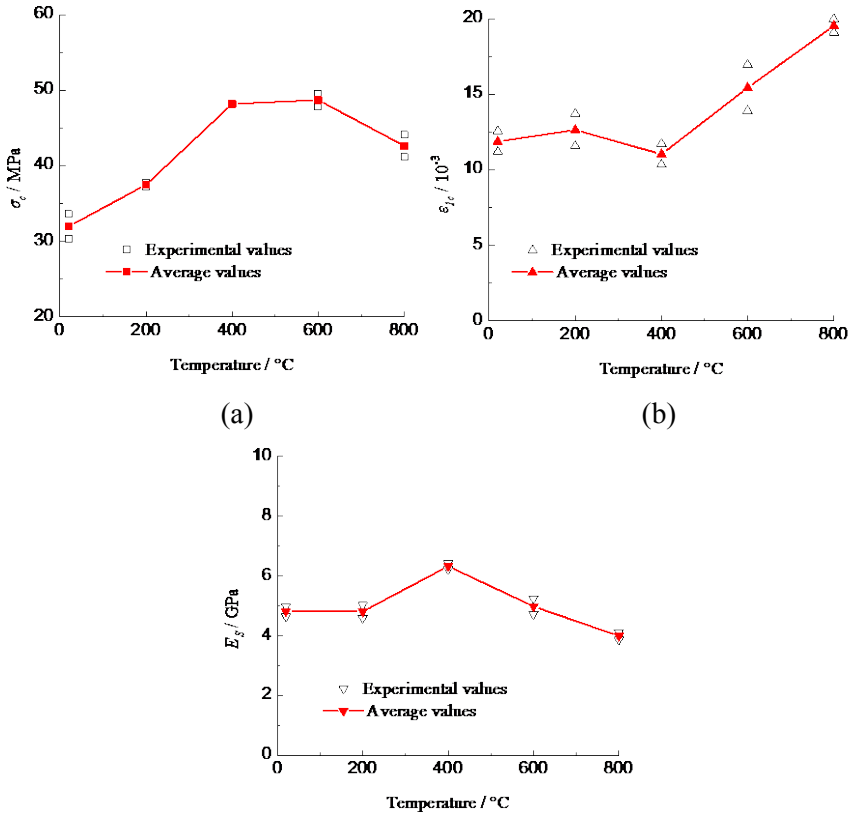

Figure 5: Effect of high temperature on the strength and deformation parameters of pre-holed sandstone specimens after heat treatment. (a) Peak strength, (b) peak strain and (c) elastic modulus

3.2 Deformation and failure process

Fig. 6 shows the stress-time-AE count curves of the sandstone specimens during the entire loading process. All the curves exhibit similar characteristics that can be divided into four periods. (1) At the initial low stress level in the nonlinear deformation period (point a), minimal AE signal can be detected, and the stress curves are smooth and concave up. Then, the stress curves show linear elastic deformation. (2) Near the first peak stress point (point b), obvious AE counts can be clearly detected, suggesting the initiation of macro-cracks. (3) During the post-peak period (point c), the curve decreases and exhibits serration,

indicating the propagation of the cracks. (4) At the last peak stress (point d), the maximum number of AE counts is detected, and rock failure occurs.

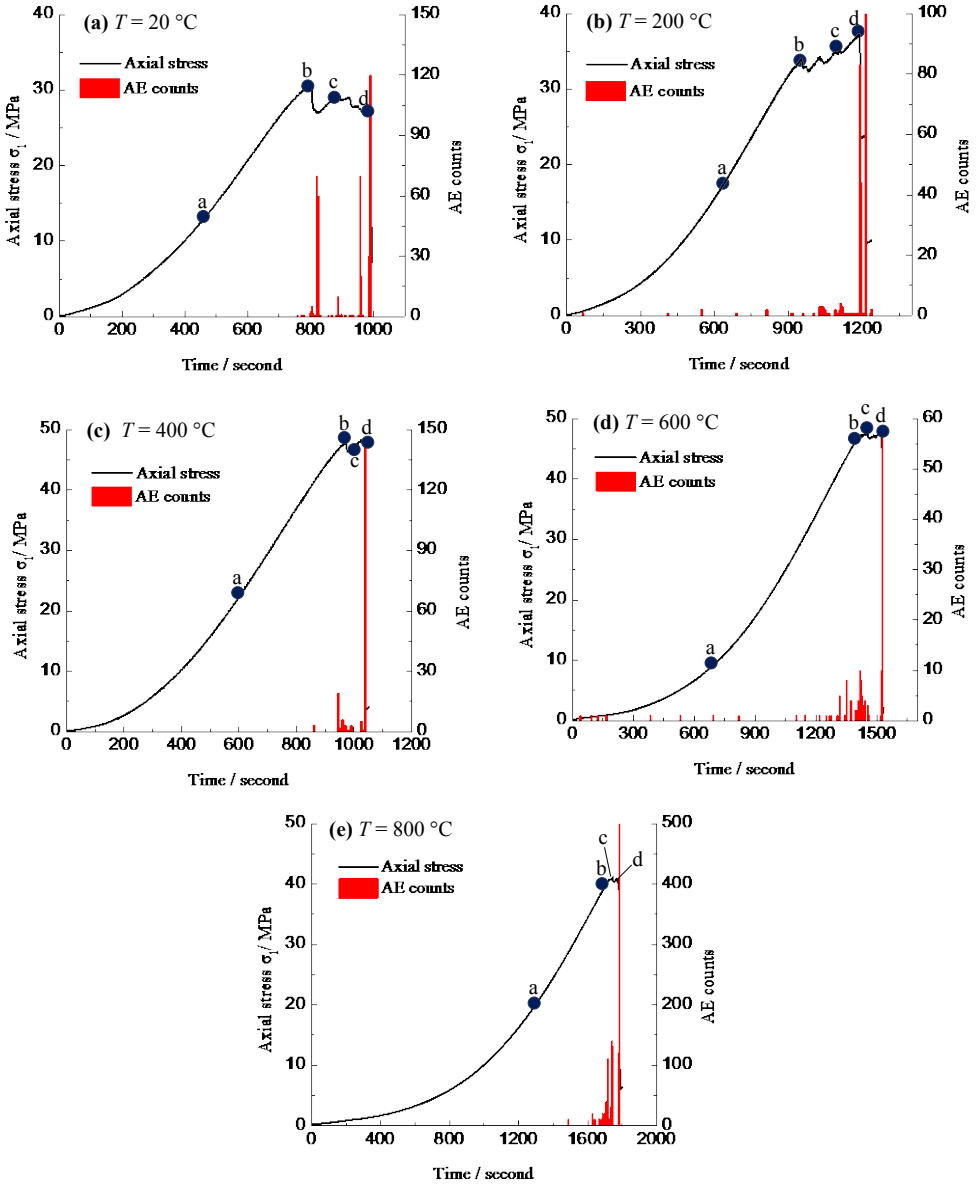

Figure 6: Stress-time-AE count curves of pre-holed sandstone specimens after heat treatment

Throughout the entire test, the whole failure process of the surface displacement was recorded by the CCD camera and then analyzed using PhotoInfor. The crack evolution process of the hole sidewalls was recorded in real-time by the microcamera.

Fig. 7 shows the deformation and failure behavior of the sandstone during the confined compression test at room temperature (20°C). At point a, there are no cracks on the surface of specimen or the sidewalls of the hole, which can be confirmed by the AE data. Only displacement in the upper part of the specimen can be observed. When the stress increases to 30.17 MPa (point b), concentrated displacement occurs in the right wall of the hole due to a high concentration of stress. The displacement does not occurs in both sides of the wall due to rock heterogeneity, such as pores, micro-cracks and the machining accuracy of the specimen. At this moment, particle ejection occurs in the sidewalls, and particles and small rock fragments can be observed in the floor. When the stress decreases to 28.38 MPa (point c), concentrated displacement is seen in both sides of the wall and spread to upward and downward in the specimen. The inner flakes on both sides experience bending and breaking, rock fragment exfoliations occurs, and large quantities of rock fragments exfoliation accumulate in the floor. Then, the rock fragment particles at point c are larger than those at point b. At point d, the final failure quickly occurs, the stress abruptly drops to 7 MPa, and the maximum AE counts is detected. Then, two V-shaped notches develop in both sides of the wall.

The damage evolution shows different characteristics limited by confined compression. Weng et al. [Weng, Li, Taheri et al. (2018)] conducted the unconfined compression tests, they found that the damage of mini-tunnels was initiated with a primary tensile crack in floor, then, shear cracks in side walls occurred.

Fig. 8 shows the deformation and failure behavior of sandstone during the confined compression test at 200°C. The first period of the 200°C sample exhibits the same characteristics as that of the room temperature. However, the second period has quite different characteristics in that both the deformation concentration and cracks inside the hole are much more severe. When the stress increases to 33.35 MPa (point c), step-like V-shaped notches occur at both sidewalls. At point d, an obvious shear zone occurs at an angle 45 degrees from the horizontal plane. V-shaped notches also develop in both sidewalls and failure occurs.

Fig. 9 shows the deformation and failure behavior of sandstone during the confined compression test at 400°C. At points a-c, the deformation and cracks inside the hole of the 400°C sample show the same trend as those of the room temperature sample. However, the final failure mode exhibits a different symmetric pattern, but the cracks inside the hole also have V-shaped notches. This phenomenon is further analyzed in detail in the following section.

Fig. 10 shows the deformation and failure behavior of the sandstone during the confined compression test at 600°C. The first and second periods of the sample at 600°C show the same trend as those of the sample at the room temperature. However, during the post-peak period (point c), the cracks inside the hole are less severe. Moreover, at points a-c, surface deformation is in a stable stage. When the specimen is loaded to point d, failure abruptly occurs. Cracks are observed in the sidewalls of the hole (point c) by the microcamera behind the specimen (Fig. 2). The displacement field cannot be seen at the sidewalls, because DSCM can only measure surface deformation. It should be noted that an axial force was imposed on the vault, resulting in obvious concentrated displacement.

Fig. 11 shows the deformation and failure behavior of the sandstone during the confined compression test at 800°C. At points a-c, the cracks inside the hole follow the same trend

as that of the room temperature sample. However, the displacement distribution extends throughout the entire specimen. A possible reason for this phenomenon is the maximum elastic modulus value of this sample, which allows the brittleness of specimens to decreases and the ductility to increase. At point d, the deformation is most concentrated at the top of the hole.

Through the above analysis of the deformation and failure behavior of the pre-holed specimens after heat treatment, certain findings can be drawn as follows:

(1) The displacement fields at different temperatures exhibit certain common phenomena: the cracks always initiate from the sidewalls of the hole and then propagate. These phenomena can be explained by the numerical simulation presented in Section 4.

(2) During the failure process, the main difference between the displacement fields of each temperature test occur in fourth period (point d), while the differences between the cracks inside the hole occur in the second period (point b), indicating that the damage on the surface lags behind the damage inside the hole.

(3) Particle ejection might be a potential indicator for failure prediction, and the severity of particle ejection is a function of the heat treatment temperature. The temperature influences the failure mode of the pre-holed sandstone after heat treatment, which indirectly influences the severity of the particle ejection.

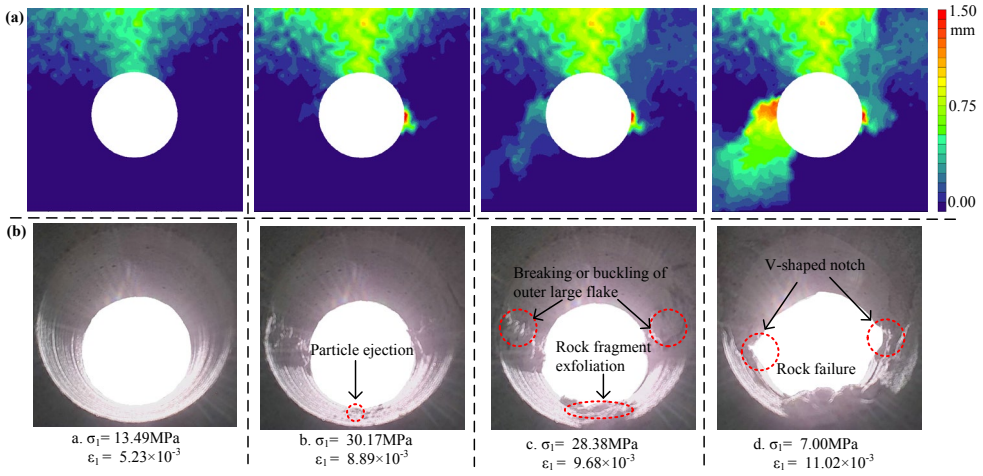

Figure 7: Deformation and failure behavior corresponding to points (a-d) in Fig. 6. (a) Displacement fields and (b) cracks inside the hole (T=20°C)

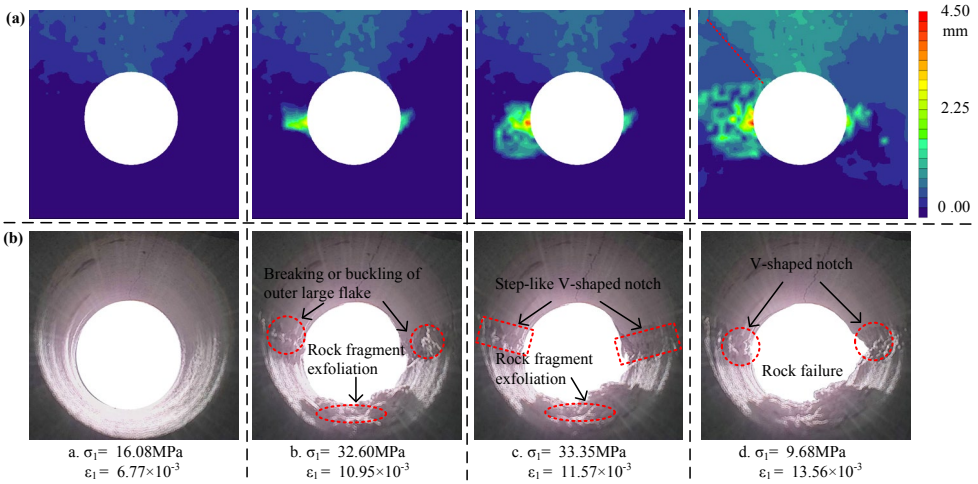

Figure 8: Deformation and failure behavior corresponding to points (a-d) in Fig. 6. (a) Displacement fields and (b) cracks inside the hole (T=200°C)

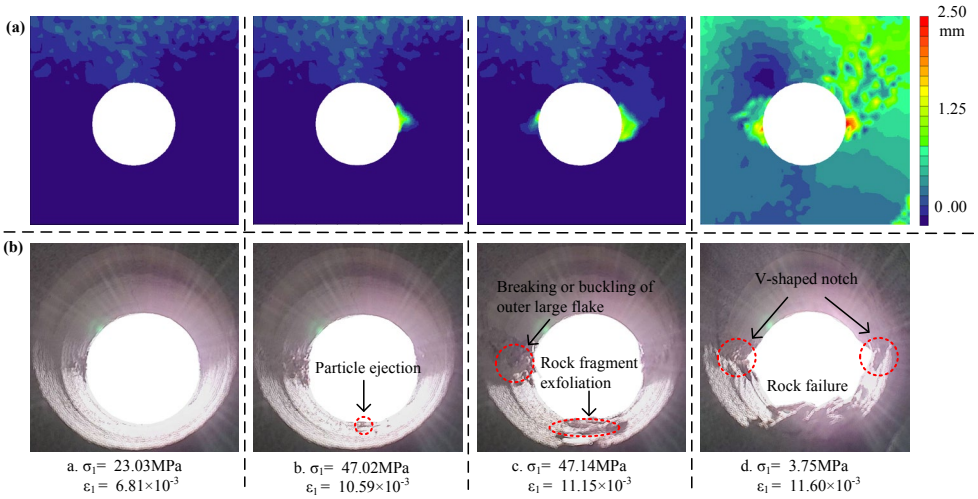

Figure 9: Deformation and failure behavior corresponding to points (a-d) in Fig. 6. (a) Displacement fields and (b) cracks inside the hole (T=400°C)

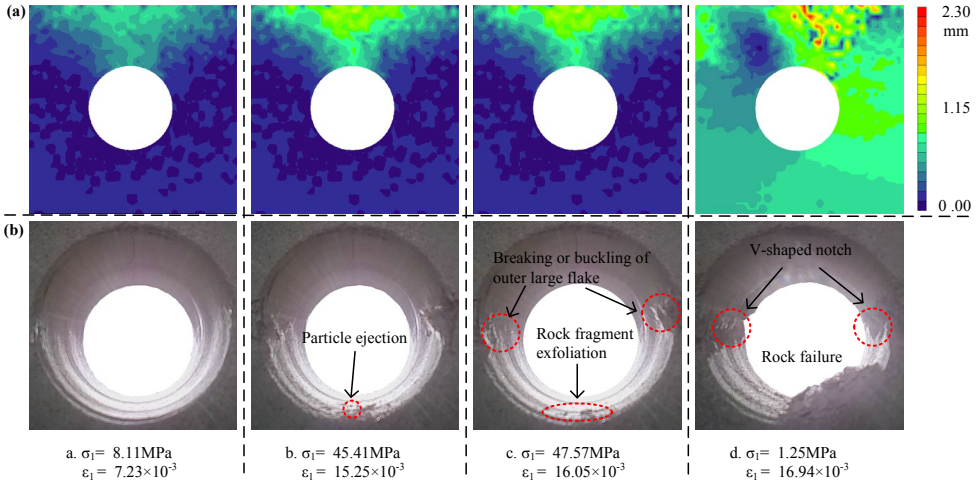

Figure 10: Deformation and failure behavior corresponding to points (a-d) in Fig. 6. (a) Displacement fields and (b) cracks inside the hole (T=600°C)

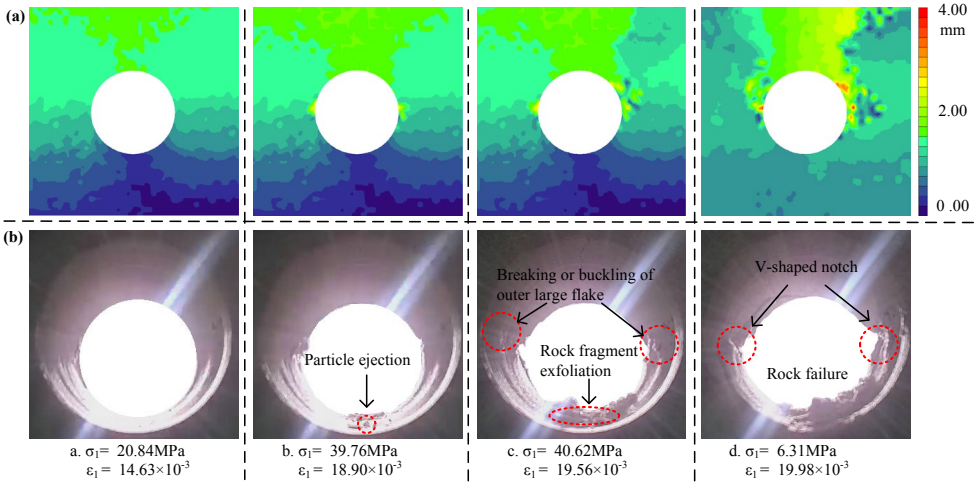

Figure 11: Deformation and failure behavior corresponding to points (a-d) in Fig. 6. (a) Displacement fields and (b) cracks inside the hole (T=800°C)

3.3 Failure modes

Fig. 12 shows the typical failure process inside the hole at each temperature: calm period, particle ejection period, rock fragment exfoliation period and rock failure period. At first, the specimens are loaded resulting in buckling of the sidewall. Then, particle ejection occurs on the sidewalls, and small rock fragments can be observed in the floor. In the post-peak period, large quantities of rock fragments are exfoliated and accumulated in the floor. The rock fragment particles are larger in this period. Finally, failure occurs with two V-shaped notches. These data are consistent with those of Hu et al. [Hu, Su, Chen et al. (2018)]. Moreover, the characteristic differences between the cracks inside the hole at each

temperature almost entirely depend on the second period (point b). The temperature of the heat treatment greatly influences the severity of cracks inside the hole.

Fig. 13 shows the final failure mode of the pre-holed sandstone after heat treatment and under confined compression. The failure modes are closely related to the heat treatment temperature, and these modes can be divided into three categories: mixed mode, shear mode and splitting mode.

At room temperature, an upward tensile crack and a downward shear crack spread from the two sidewalls to the top and bottom specimen surfaces, respectively, exhibiting a mixed failure mode. The failure mode of the room temperature specimen can be classified as a mix of shear and tensile failure (Fig. 13(a)).

At 200°C, as the displacement field shows, an obvious shear zone occurs at an angle 45 degrees from the horizontal plane, resulting in shear failure. Shear cracks dominate the final failure, so the failure mode of the 200°C specimen is shear failure.

At 400°C, 600°C and 800°C, the final failure mode is quite different from those of the above specimens. The asymmetric failure just occurs in the upper part of the specimens and spreads near the hole. Tensile cracks and surface spalling dominate the final failure, which is a splitting failure. As shown in Fig. 4, the specimen experiences brittle failure, which is different from the failure of room temperature and 200°C specimens, where the curve slowly decreases after the peak stage. It is reasonable to confirm that the heat treatment temperatures influence the failure mode of the pre-holed sandstone specimens under confined compression.

With increasing treatment temperature, the failure mode changes from mixed and shear mode to a splitting mode. Furthermore, after heat treatment, the specimens have different final failure features for the entire rock, but have the same failure features inside the hole. These phenomena can be explained by the numerical simulation presented in the following section.

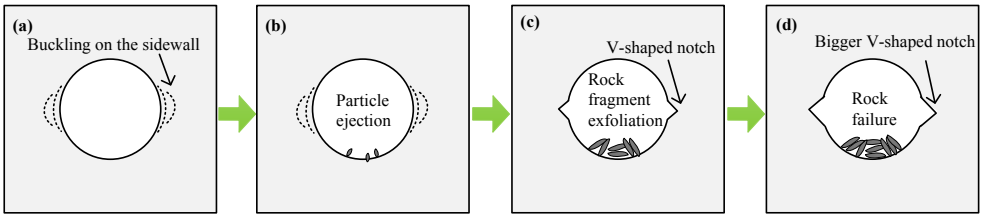

Figure 12: Schematic diagram of common failure process inside the hole at each temperature. (a) Calm period, (b) particle ejection period, (c) rock fragment exfoliation period and (d) rock failure period

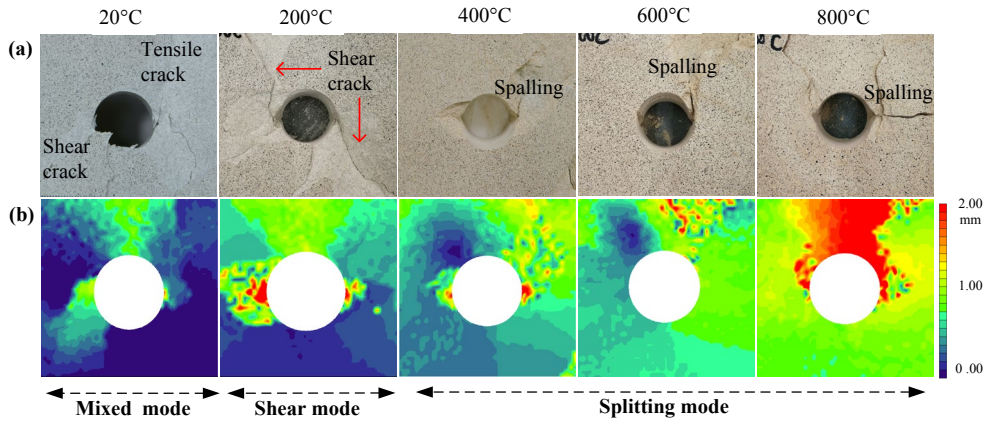

Figure 13: Final failure mode of pre-holed sandstone after heat treatment and under confined compression. (a) Failure image and (b) displacement fields

4 Numerical modeling of damage evolution

4.1 Numerical model construction

To verify the results of the laboratory tests, as well as further explore the failure mechanism, numerical simulations were conducted using FLAC^{3D} (Fast Lagrangian Analysis of a Continua in 3 Dimensions) [Gong and Guo (2019)]. The basic mechanical parameters used for the simulation are listed in Tab. 1. The plastic strain ratio represents the equivalent critical plastic strain. The yield ratio and elastic reduction ratio represent characteristics of the pre-peak and post-peak stages.

The temperature-induced changes in the parameter have important influences on the rock damage, which is analyzed in Sections 3.1 and 5. Thus, temperature effect can be simulated by a damage model. As shown in Fig. 14, a damage-softening constitutive model [Xu (2018)] was used to simulate the rock damage after thermal treatment based on the parameters from the laboratory tests.

FLAC^{3D} is an effective finite difference method for damage evolution analysis. The finite difference work is to get the relationship between the strain increment and the stress increment. The elastic relation between the elastic strain increments and stress increments is as follows:

$$\{\boldsymbol{\sigma}^e\}_N = \{\boldsymbol{\sigma}^e\}_I + [\boldsymbol{D}]\{\Delta\boldsymbol{\varepsilon}\}_I \tag{1}$$

where $\{\sigma^e\}_I$ is the stress matrix before update, $\{\sigma^e\}_N$ is the stress matrix after update, $\{\Delta\varepsilon\}_I$ is the matrix of the strain increment, and $[D]$ is the unit stiffness.

Then determine whether the units reach yield based on the equivalent Mohr-Coulomb yield criterion:

$$f^s = \sigma_1 - \frac{1+\sin\varphi}{1-\sin\varphi}\sigma_3 + \frac{2\cos\varphi}{1-\sin\varphi}C \tag{2}$$

The failure criterion of tension is

$$g^t = \sigma_3 - \sigma^t \tag{3}$$

$$\sigma^t \le 1/2\,\sigma_c\left(m - \left(m^2+4\right)^{1/2}\right) \tag{4}$$

On the yield surface, the locations of the shear failure and tensile failure are determined as:

$$h = \sigma_3 - \sigma^t + a^p\left(\sigma_1 - \sigma^p\right) \tag{5}$$

$$a^p = \sqrt{1+\left(\frac{1+\sin\varphi'}{1-\sin\varphi'}\right)^2} + \frac{1+\sin\varphi'}{1-\sin\varphi'} \tag{6}$$

$$\sigma^p = \sigma^t\frac{1+\sin\varphi'}{1-\sin\varphi'} - 2c'\sqrt{\frac{1+\sin\varphi'}{1-\sin\varphi'}} \tag{7}$$

where φ' is the equivalent internal friction angle, and m_i is the experiential parameter.

When f^s>0 and h>0, the units are in the elastic stage, the mechanical parameters of the rock material should be maintained.

When f^s<0 and h>0, the units need to correct stress to the shear and tensile yield surface. The corrected stress is

$$\begin{cases} \sigma_1^N = \sigma_1^I - \lambda^s\left(\alpha_1 - \alpha_2 N_\psi\right) \\ \sigma_2^N = \sigma_2^I - \lambda^s\alpha_2\left(1 - N_\psi\right) \\ \sigma_3^N = \sigma_3^I - \lambda^s\left(-\alpha_1 N_\psi + \alpha_2\right) \end{cases} \tag{8}$$

where

$$\begin{cases} \alpha_1 = K + \dfrac{4}{3}G \\ \alpha_2 = K - \dfrac{2}{3}G \end{cases} \tag{9}$$

$$\lambda^s = \frac{f^s\left(\sigma_1^I, \sigma_3^I\right)}{\left(\alpha_1 - \alpha_2 N_\psi\right) - \left(-\alpha_1 N_\psi + \alpha_2\right)N_\varphi} \tag{10}$$

$$\begin{cases} N_\varphi = \left(1+\sin\varphi\right)/\left(1-\sin\varphi\right) \\ N_\psi = \left(1+\sin\psi\right)/\left(1-\sin\psi\right) \end{cases} \tag{11}$$

where K is the shear modulus, G is the bulk modulus, φ is the internal friction angle, and ψ is the dilatancy angle.

Derived from these equations, we obtain $\Delta\varepsilon_{ij}^{ps}$ (Shear plastic increment):

$$\begin{cases} \Delta\varepsilon_1^{ps} = \lambda^s \\ \Delta\varepsilon_2^{ps} = 0 \\ \Delta\varepsilon_3^{ps} = -N_\psi\lambda^s \end{cases} \tag{12}$$

When g^t<0 and h≤0, the units need to correct stress to the tensile yield surface. The corrected stress is

$$\begin{cases} \sigma_1^N = \sigma_1^I - \lambda^t \alpha_2 \\ \sigma_2^N = \sigma_2^I - \lambda^t \alpha_2 \\ \sigma_3^N = \sigma_3^I - \lambda^t \alpha_1 \end{cases} \tag{13}$$

$$\lambda^t = \frac{\sigma_3^I - \sigma^t}{\alpha_1} \tag{14}$$

we obtain $\Delta\boldsymbol{\varepsilon}_{ij}^{pt}$ (Tensile plastic increment)

$$\begin{cases} \Delta\varepsilon_1^{pt} = 0 \\ \Delta\varepsilon_2^{pt} = 0 \\ \Delta\varepsilon_3^{pt} = \lambda^t \end{cases} \tag{15}$$

Finally, the evolution equation of the damage variable, D^t (Tensile damage variable) and D^s (Shear damage variable), are defined as follows:

$$\begin{cases} D^s = \dfrac{\varepsilon^{ps}}{\varepsilon^{psL}} & \left(\varepsilon^{ps} < \varepsilon^{psL}\right) \\ D^s = 1.0 & \left(\varepsilon^{ps} \geq \varepsilon^{psL}\right) \end{cases} \tag{16}$$

$$\begin{cases} D^t = 0 & \left(\varepsilon^{pt} = 0\right) \\ D^t = 1.0 & \left(\varepsilon^{pt} > 0\right) \end{cases} \tag{17}$$

The numerical modeling agrees with the laboratory tests. The comparison figures between experimental test and numerically modeled uniaxial compression tests are shown in Fig. 15. Though there are apparent gaps between the simulation curves and laboratory curves, the two elastic stages are approximate. At the beginning of the laboratory tests, there is a compaction stage with a concave curve because of the closure of the original micro-cracks due to the loading force. The boundary conditions and loading process of the numerical model were same as those of the laboratory tests.

Table 1: Basic mechanical parameters of the simulation model

Treatment temperature	Cohesion (MPa)	Internal friction angle (°)	Elastic modulus (MPa)	Poisson's ratio	Tensile strength (MPa)	Dilation (°)	Plastic strain ratio	Yield ratio	Elastic reduction ratio
20°C	9.2	45	6.1	0.24	3.31	6	0.005	0.9	1
200°C	10.3	42	5.6	0.20	3.48	5.6	0.012	0.8	0.7
800°C	11.6	44	4.4	0.22	3.5	5.9	0.013	0.8	0.7

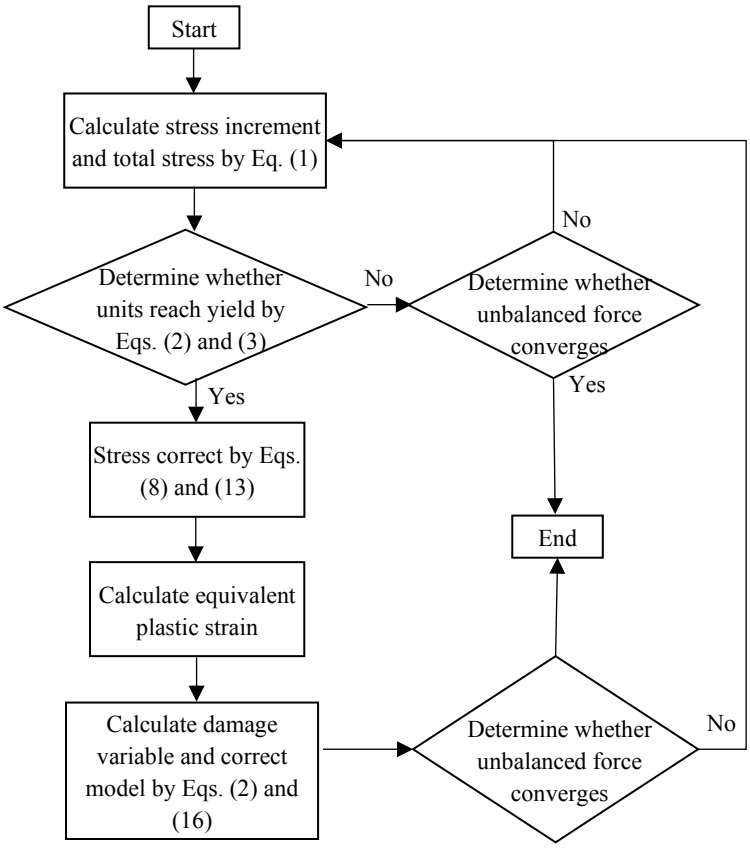

Figure 14: Damage-softening constitutive model in FLAC^{3D} [Xu (2018)]

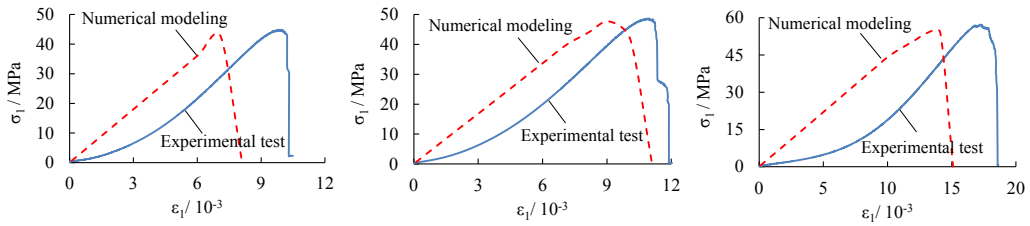

(a) T=20°C (b) T=200°C (c) T=800°C

Figure 15: Comparison between experimental test and numerically modeled uniaxial compression tests

4.2 Damage evolution

Fig. 16 shows the damage evolution in terms of the per-damage. The per-damage represents the degree of damage at every time step. Initially, the three temperatures exhibit the same trend of increasing with the calculation time step. As shown in Fig. 17, damage always first

occurs at sidewalls of the hole and then spreads horizontally. The cracks inside the hole captured by the microcamera exhibited the same characteristics (Fig. 12).

When the specimen is loaded to point b, as the heated treatment temperature increases, the damage curves exhibit a relatively greater slope. As shown in Fig. 17, the damage zone gradually extends from the sidewalls to the horizontal boundary. Notably, at 20°C, damage zones emerge far from the hole at the four corners and then propagate.

When the specimen is loaded to point c and d, at 20°C, both the shear and tensile damage zones gradually propagate and then coalesce at the damage zone of sidewall of the hole. At 800°C, the slope of per-damage curve experiences recesses (Fig. 16), because tensile splitting dominates the failure process, while at 20°C and 200°C, shear cracks result in more serious damage. The top of the hole experiences a remote damage zone, which is mainly caused by shear damage.

In Fig. 18(a), the yellow and red zones represent the shear and tensile damage zones respectively. The failure modes change from mixed and shear modes to a splitting mode with increasing treatment temperature, which is consistent with the experimental results (Fig. 13). At 20°C, both shear and tensile failure are initiated from sidewalls of the hole exhibiting a mixed mode. At 200°C, an obvious shear zone leads to the final failure. At 800°C, unsymmetrical failure only occurs in the upper part of specimen, and tensile cracks and surface spalling (Fig. 13) dominate the final failure, which is a splitting failure mode.

Damage zones always occur at sidewalls of the hole and then propagate to the entire rock affected by shear or tensile damage. As shown in Fig. 18(b), the ordinate represents the ratio of the shear to tensile zones. From 20°C to 200°C, the proportion of the final failure increases, while the past failure decreases, suggesting that the thermal effect promote shear damage and restrain tensile damage. From 200°C to 800°C, it exhibits the opposite trend that the thermal effect promotes tensile damage and restrains shear damage. Thus, the final damage pattern of the rock depends on the temperature range.

In particular, the damage zone near sidewalls of the hole has the same distribution range and pattern at all temperatures. Although the damage pattern of the surrounding rock is different, the samples have similar characteristics near sidewalls of the hole exhibiting V-shaped notches (Fig. 12).

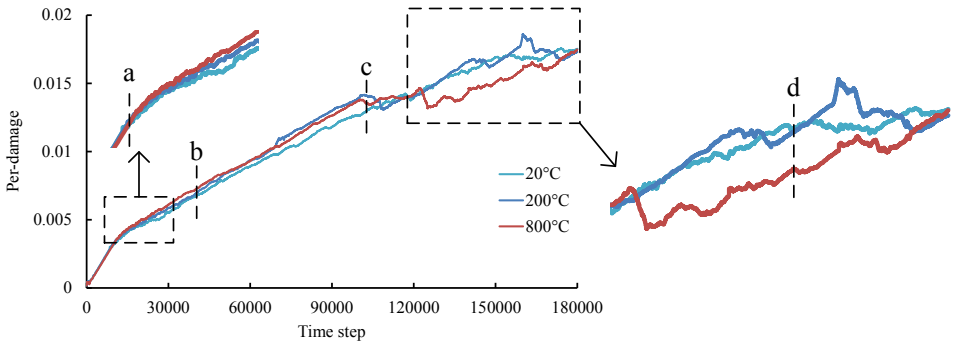

Figure 16: Damage evolution of per-damage curves

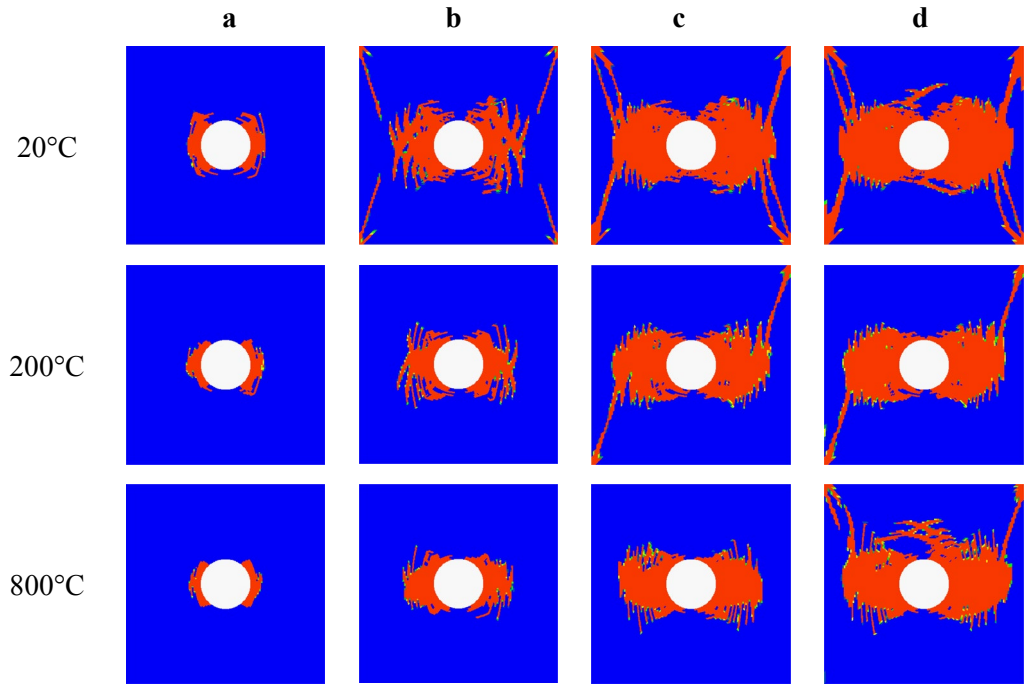

Figure 17: Evolution of damage zone corresponding to points (a-d) in Fig. 16

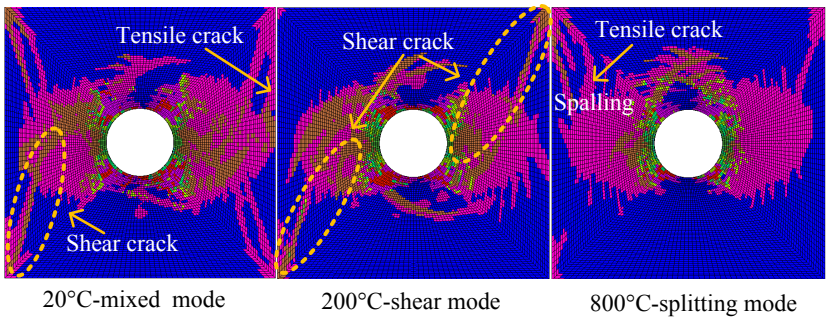

(a)

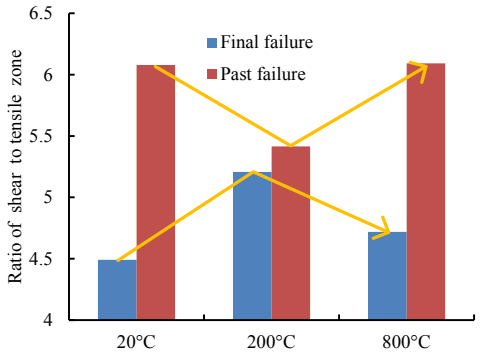

(b)

Figure 18: Failure mode of pre-holed sandstone after heat treatment and under confined compression. (a) Plastic zone distribution and (b) ratio of shear to tensile zone with respect to the temperature

5 Discussion

To support and analyze the influence of the heat treatment temperature on the sandstone specimens, the microstructural morphology of the sandstone after each thermal treatment was investigated to study the associated mechanism. The microstructural characteristics of the sandstone after thermal treatment can be revealed via SEM analysis.

The composition and internal structure directly affect the mechanical properties of the rock material [Sun, Zhang, Zhu et al. (2019)]. As shown in Fig. 19, at room temperature, original cracks such as grain boundary cracks are present. When the temperature increases to 200°C, 400°C and 600°C, the specimens have almost no cracks and exhibit a compact microstructure. Thermal expansion of the mineral grains closes the original cracks; thus, high-temperature treatment strengthens the sandstone specimens' strength. When the temperature increases to 800°C, the strength of the specimen abruptly decreases, so 600°C is the temperature threshold for this study. Su et al. [Su, Wei, Qin et al. (2017a)] demonstrated a similar trend in experimental studies.There is strong evidence of melting on the quartz surface, suggesting that high temperature greatly influences the mineral grains. In addition to grain boundary cracks, trans-granular micro cracks begin to emerge. The width of cracks from 800°C treatment is greater than those for the other temperature treatment, suggesting that the 800°C treatment causes more serious damage. Connected cracks are also be observed, mainly resulting from the thermal expansion of mineral grains and partly resulting from a phase transition. Quartz has a phase transition from α to β phase at 573°C, where the volume rapidly increases [Su, Wei, Qin et al. (2017a)], and the mineral cements and components change with increasing temperature, which possibly affects the deformation behavior of the specimen.

Through energy dispersive spectrometer (EDS) analysis, the elemental distributions of the minerals can be obtained. As shown in Fig. 20, Fe presents a gathering pattern in 20°C sample. In 200°C sample, the Fe gathered area is a smaller area. As the increasing treatment temperature, concentration capacity of the Fe decreases. From the XRD results (Fig. 1(b)),

the Fe is provided by the siderite, which probably changes components due to the high-temperature treatment. This effect could explain why the specimen colour changes with the heat treatment temperature.

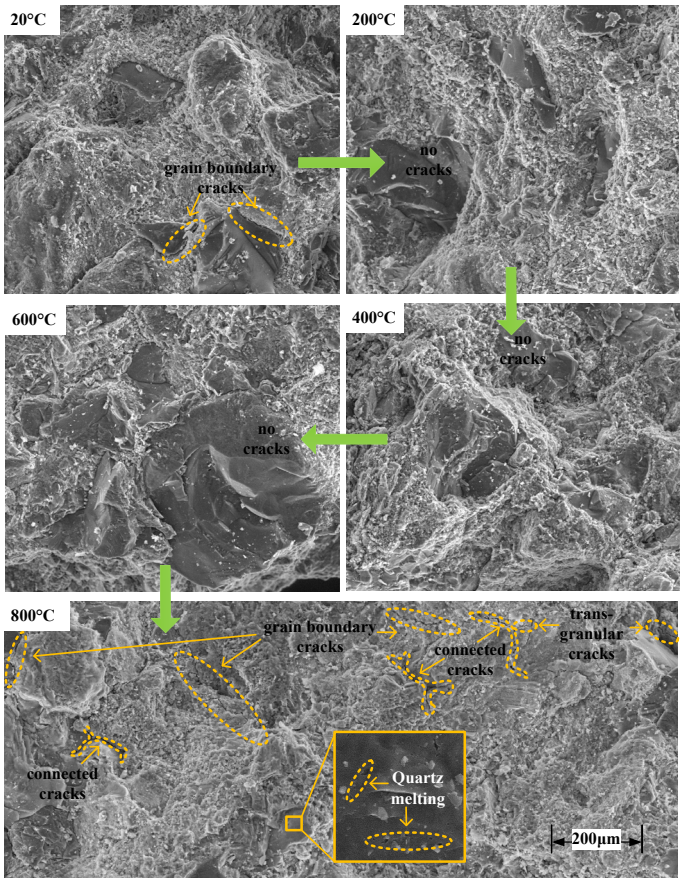

Figure 19: SEM images of the sandstone specimens after heat treatment

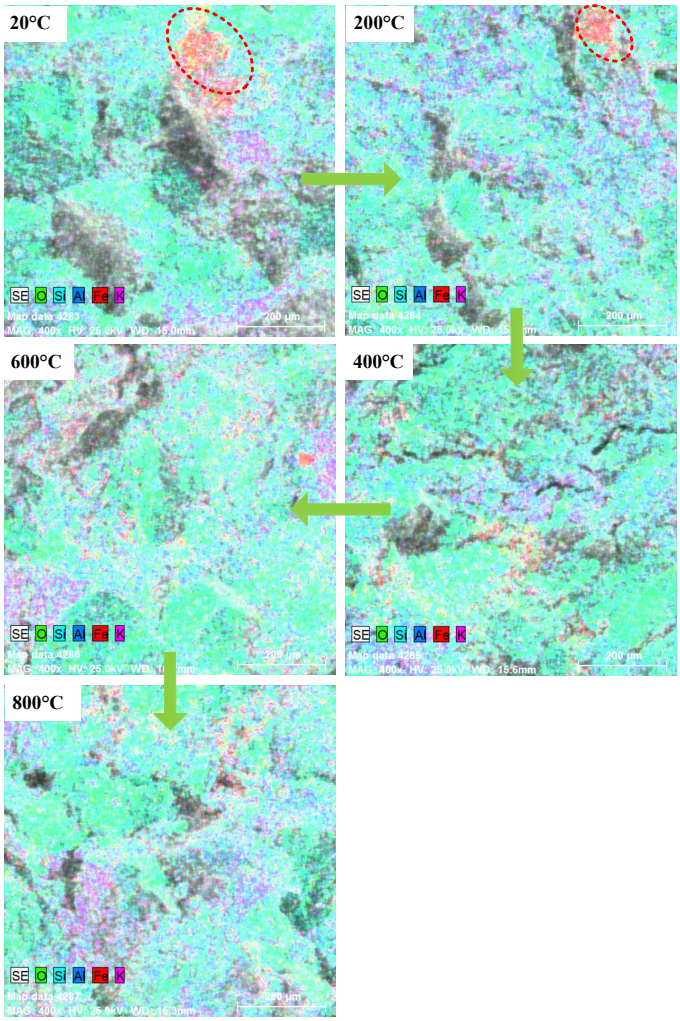

Figure 20: EDS images of sandstone specimens after heat treatment

6 Conclusions

In this study, laboratory confined compression tests and numerical simulations were conducted on pre-holed sandstone specimens after heat treatment. The physical mechanical properties, deformation and damage evolution of the specimens were analyzed. The conclusions can be summarized as follows:

(1) The failure modes are closely related to the heat treatment temperature, and can be divided into three categories: mixed mode, shear mode and splitting mode. With increasing treatment temperature, the failure mode changes from tensile and shear modes to a splitting mode. The cracks always initiate from sidewalls of the hole and then propagate.

(2) The failure process inside the hole can be described as follows: calm period, particle ejection period, rock fragment exfoliation period and rock failure period. During the failure process, the main difference between the displacement fields of each temperature test occurs in the fourth period, while the difference between the cracks inside the hole occurs in the second period. The specimens have different final failure features over the entire rock, but have the same failure features inside the hole after heat treatment.

(3) The failure modes of the numerical results agree very well with those observed in the experimental results. The damage zone always occurs at sidewalls of the hole and then propagates to the entire rock affected by shear or tensile damage. From 20°C to 200°C, the thermal effect may promote shear damage and restrain tensile damage. From 200°C to 800°C, the thermal effect promotes tensile damage and restrains shear damage. In particular, the damage zone near the sidewalls of the hole has the same distribution range and pattern.

Acknowledgement: This research was supported by the National Basic Research Program of China (973 Program) Grant No. 2014CB046905 and the National Natural Science Foundation of China (No. 51174197). Additionally, the authors are grateful to the anonymous reviewers of this article for their careful reading of the manuscript and their many helpful comments.

Conflicts of Interest: The authors declare that they have no conflicts of interest to report regarding the present study.

References

Akdag, S.; Karakus, M.; Taheri, A.; Nguyen, G.; Manchao, H. (2018b): Effects of thermal damage on strain burst mechanism for brittle rocks under true-triaxial loading conditions. *Rock Mechanics and Rock Engineering*, vol. 51, pp. 1657-1682.

Chen, G.; Li, T.; Zhang, G.; Yin, H.; Zhang, H. (2014): Temperature effect of rock burst for hard rock in deep-buried tunnel. *Natural Hazards*, vol. 72, no. 2, pp. 915-926.

Chen, G.; Li, T.; Li, G.; Qin, C. A.; He, Y. (2018): Influence of temperature on the brittle failure of granite in deep tunnels determined from triaxial unloading tests. *European Journal of Environmental and Civil Engineering*, vol. 22, no. 1, pp. 269-285.

Chen, M.; Yang, S.; Pathegama, G. R.; Yang, W.; Yin, P. et al. (2018): Fracture processes of rock-like specimens containing nonpersistent fissures under uniaxial compression. *Energies*, vol. 12, no. 1, pp. 79.

Chen, Y. L.; Ni, J.; Shao, W.; Azzam, R. (2012): Experimental study on the influence of temperature on the mechanical properties of granite under uni-axial compression and fatigue loading. *International Journal of Rock Mechanics & Mining Sciences*, vol. 56, no. 15, pp. 62-66.

Dwivedi, R. D.; Goel, R. K.; Prasad, V. V. R.; Sinha, A. (2008): Thermo-mechanical properties of Indian and other granites. *International Journal of Rock Mechanics & Mining Sciences*, vol. 45, no. 3, pp. 303-315.

Gong, F. Q.; Si, X. F.; Li, X. B.; Wang, S. Y. (2018): Experimental investigation of strain rockburst in circular caverns under deep three-dimensional high-stress conditions. *Rock Mechanics and Rock Engineering*, vol. 52, no. 5, pp. 1-16.

Gong, Y.; Guo, G. (2019): A data-intensive FLAC (3D) computation model: application of geospatial big data to predict mining induced subsidence. *Computer Modeling in Engineering & Sciences*, vol. 119, no. 2, pp. 395-408.

Haimson, B.; Chang, C. (2000): A new true triaxial cell for testing mechanical properties of rock, and its use to determine rock strength and deformability of Westerly granite. *International Journal of Rock Mechanics & Mining Sciences*, vol. 37, no. 1, pp. 285-296.

Heuze, F. E. (1983): High-temperature mechanical, physical and thermal properties of granitic rocks-a review. *International Journal of Rock Mechanics & Mining Sciences & Geomechanics Abstracts*, vol. 20, no. 1, pp. 3-10.

Hu, X.; Su, G.; Chen, G.; Mei, S.; Feng, X. et al. (2018): Experiment on rockburst process of borehole and its acoustic emission characteristics. *Rock Mechanics and Rock Engineering*, vol. 52, no. 3, pp. 783-802.

Huang, Y. H.; Yang, S. Q.; Tian, W. L.; Zhao, J.; Ma, D. et al. (2017): Physical and mechanical behavior of granite containing pre-existing holes after high temperature treatment. *Archives of Civil & Mechanical Engineering*, vol. 17, no. 4, pp. 912-925.

Huang, N.; Liu, R.; Jiang, Y.; Cheng, Y.; Li, B. (2019): Shear-flow coupling characteristics of a three-dimensional discrete fracture network-fault model considering stress-induced aperture variations. *Journal of Hydrology*, vol. 571, pp. 416-424.

Kong, B.; Wang, E.; Li, Z.; Wang, X.; Jie, L. et al. (2016): Fracture mechanical behavior of sandstone subjected to high-temperature treatment and its acoustic emission characteristics under uniaxial compression conditions. *Rock Mechanics & Rock Engineering*, vol. 49, no. 12, pp. 1-8.

Kumari, W. G. P.; Ranjith, P. G.; Perera, M. S. A.; Shao, S.; Chen, B. K. et al. (2017): Mechanical behavior of Australian Strathbogie granite under in-situ stress and temperature conditions: an application to geothermal energy extraction. *Geothermics*, vol. 65, pp. 44-59.

Kusui, A.; Villaescusa, E.; Funatsu, T. (2016): Mechanical behavior of scaled-down unsupported tunnel walls in hard rock under high stress. *Tunnelling and Underground Space Technology*, vol. 60, pp. 30-40.

Lee, H.; Moon, T.; Haimson, B. C. (2015): Borehole breakouts induced in arkosic sandstones and a discrete element analysis. *Rock Mechanics & Rock Engineering*, vol. 49, no. 4, pp. 1369-1388.

Li, Y.; Tang, X.; Yang, S.; Chen, J. (2019): Evolution of the broken rock zone in the mixed ground tunnel based on the DSCM. *Tunnelling and Underground Space Technology*, vol. 84, pp. 248-258.

Li, Y.; Zhang, Q.; Lin, Z.; Wang, X. (2016): Spatiotemporal evolution rule of rocks fracture surrounding gob-side roadway with model experiments. *International Journal of Mining Science & Technology*, vol. 26, no. 5, pp. 895-902.

Liu, X.; Liang, Z.; Zhang, Y.; Liang, P.; Tian, B. (2018): Experimental study on the monitoring of rockburst in tunnels under dry and saturated conditions using AE and infrared monitoring. *Tunnelling and Underground Space Technology*, vol. 82, pp. 517-528.

Martín-Gamboa, M.; Iribarren, D.; Dufour, J.; Martín-Gamboa, M.; Iribarren, D. (2015): On the environmental suitability of high- and low-enthalpy geothermal systems. *Geothermics*, vol. 53, no. 4, pp. 27-37.

Minissale, A.; Borrini, D.; Montegrossi, G.; Orlando, A.; Tassi, F. et al. (2008): The Tianjin geothermal field (north-eastern China): water chemistry and possible reservoir permeability reduction phenomena. *Geothermics*, vol. 37, pp. 400-428.

Mohamadi, M.; Wan, R. G. (2016): Strength and post-peak response of Colorado shale at high pressure and temperature. *International Journal of Rock Mechanics and Mining Sciences*, vol. 84, pp. 34-46.

Su, G.; Chen, Z.; Ju, J. W.; Jiang, J. (2017): Influence of temperature on the strainburst characteristics of granite under true triaxial loading conditions. *Engineering Geology*, vol. 222, pp. 38-52.

Su, C. D.; Wei, S. J.; Qin, B. D.; Yang, Y. S. (2017a): Experimental study of influence mechanism of high temperature on mechanical properties of fine-grained sandstone. *Rock & Soil Mechanics*, vol. 38, no. 3, pp. 623-630.

Su, H.; Jing, H.; Yin, Q.; Yu, L.; Wang, Y. et al. (2017b): Strength and deformation behaviors of veined marble specimens after vacuum heat treatment under conventional triaxial compression. *Acta Mechanica Sinica*, vol. 33, pp. 886-898.

Sun, Q.; Zhang, W.; Zhu, Y.; Huang, Z. (2019): Effect of high temperatures on the thermal properties of granite. *Rock Mechanics and Rock Engineering*, pp. 1-9.

Taheri, A.; Royle, A.; Yang, Z.; Zhao, Y. (2016): Study on variations of peak strength of a sandstone during cyclic loading. *Geomechanics and Geophysics for Geo-Energy and Geo-Resources*, vol. 2, no. 1, pp. 1-10.

Weng, L.; Li, X.; Taheri, A.; Wu, Q.; Xie, X. (2018): Fracture evolution around a cavity in brittle rock under uniaxial compression and coupled static-dynamic loads. *Rock Mechanics and Rock Engineering*, vol. 51 no. 2, pp. 531-545.

Xu, P. (2018): *Study on Rheological Behavior of Deep Buried Composite Rock and Its Influencing Mechanism on TBM Jamming Disaster (Ph.D. Thesis)*. China University of Mining and Technology, China.

Yang, S. Q.; Huang, Y. H.; Tian, W. L.; Yin, P. F.; Jing, H. W. (2019): Effect of high temperature on deformation failure behavior of granite specimen containing a single fissure under uniaxial compression. *Rock Mechanics and Rock Engineering*, pp. 1-21.

Yang, S. Q.; Jing, H. W.; Huang, Y. H.; Ranjith, P. G.; Jiao, Y. Y. (2014): Fracture mechanical behavior of red sandstone containing a single fissure and two parallel fissures after exposure to different high temperature treatments. *Journal of Structural Geology*, vol. 69, pp. 245-264.

Yao, M.; Rong, G.; Zhou, C.; Peng, J. (2016): Effects of thermal damage and confining pressure on the mechanical properties of coarse marble. *Rock Mechanics and Rock Engineering*, vol. 49, no. 6, pp. 2043-2054.

Yin, T.; Li, X.; Yin, Z.; Zhou, Z.; Liu, X. (2012): Study and comparison of mechanical properties of sandstone under static and dynamic loadings after high temperature. *Chinese Journal of Rock Mechanics and Engineering*, vol. 31, no. 2, pp. 273-279.

Zhang, J.; Deng, H.; Taheri, A.; Ke, B.; Liu, C. et al. (2018): Degradation of physical and mechanical properties of sandstone subjected to freeze-thaw cycles and chemical erosion. *Cold Regions Science and Technology*, vol. 155, pp. 37-46.

Zeng, W.; Yang, S. Q.; Tian, W. L. (2018): Experimental and numerical investigation of brittle sandstone specimens containing different shapes of holes under uniaxial compression. *Engineering Fracture Mechanics*, vol. 200, pp. 430-450.

Zhao, C.; Niu, J.; Zhang, Q.; Zhao, C.; Zhou, Y. (2019): Failure characteristics of rock-like materials with single flaws under uniaxial compression. *Bulletin of Engineering Geology and the Environment*, vol. 78, no. 1, pp. 593-603.

Zhao, C.; Zhou, Y.; Zhao, C.; Bao, C. (2018): Cracking processes and coalescence modes in rock-like specimens with two parallel pre-existing cracks. *Rock Mechanics and Rock Engineering*, vol. 51, no. 11, pp. 3377-3393.

Zhu, Z. N.; Tian, H.; Jiang, G. S.; Cheng, W. (2018): Effects of high temperature on the mechanical properties of chinese marble. *Rock Mechanics & Rock Engineering*, vol. 51, no. 6, pp. 1937-1942.